Impurity-induced modulations in $NbSe_3$ detected by atomic-force microscopy

Y. Gong, Q. Xue, D. L. Drake, J. Qian, and R. V. Coleman*
Physics Department, University of Virginia, Charlottesville, Virginia 22901
(Received 21 September 1994; revised manuscript received 6 February 1995)

Long-range modulations at room temperature in $NbSe_3$ doped with interstitial impurities have been observed using both atomic-force microscopy and scanning tunneling microscopy. The wavelength of these modulations is a function of the impurity concentration starting as high as ten unit cells in wavelength and changing through a sequence of wavelengths to a wavelength of two unit cells. These modulations are closely connected to the existence of a strong susceptibility anomaly which induces two charge-density waves (CDW's) with onset temperatures of 144 and 59 K, respectively. If the CDW's are quenched above certain critical concentrations, then the room-temperature modulations are also quenched. This general behavior has been observed for eight different interstitial impurities: V, Mn, Cr, Gd, Pd, Fe, Co, and Ni. The impurity-induced modulations are not observed for substitutional impurities such as Ti. In a number of cases interstitial impurities at certain critical concentrations can introduce crystal phases which exhibit a range of electronic properties such as a metal-insulator transition. The presence of the high-temperature modulations has only small effects on CDW formation until the concentration approaches critical values. These effects have been monitored by measuring the temperature dependence of resistance in the range 300–4.2 K. The high-temperature modulations result from long-range impurity screening effects and preferred interstitial impurity sites, in the presence of a complex susceptibility response of the electron gas.

I. INTRODUCTION

A study of doped $NbSe_3$ at room temperature using an atomic-force microscope (AFM) has detected the presence of a variety of lattice modulations that we suggest result from long-range impurity screening effects and preferred interstitial impurity sites. These modulations develop in systems which at lower temperatures undergo a transition to a charge-density-wave (CDW) state and have complex electric susceptibilities leading to long-range ripples in the screening charge associated with the impurities.

In the case of the quasi-one-dimensional metal $NbSe_3$, two CDW phase transitions, with onset temperatures of $T_{C1}=144$ K and $T_{C2}=59$ K are observed.[1,2] Pure $NbSe_3$ has a monoclinic crystal structure with six chains per unit cell, and a number of band-structure calculations[3,4] for the high-temperature phase have been published.

Previous scanning tunneling microscope (STM) studies of pure $NbSe_3$ at 4.2 K have shown strong electronic charge modulations induced by the CDW's. These are located on different chains of the unit cell, and the observed modulations are in agreement with independently measured[5] wave vectors Q of the CDW's, which have been determined to be equal to

$$\mathbf{Q}=(0\mathbf{G}_a,0.243\mathbf{G}_b,0\mathbf{G}_c)$$

for the high-temperature CDW, and

$$\mathbf{Q}=(0.5\mathbf{G}_a,0.263\mathbf{G}_b,0.5\mathbf{G}_c)$$

for the low-temperature CDW. Here $\mathbf{G}_a$, $\mathbf{G}_b$, and $\mathbf{G}_c$ are the three reciprocal-lattice vectors of the monoclinic structure; $\mathbf{G}_b$ is along the twofold axis (chain axis).

The STM results at 4.2 K show equally strong modulations associated with the low-temperature CDW to exist on two of the three chains per surface unit cell. This observation was not expected since previous models[6,7] and nuclear-magnetic-resonance results[8] have generally concluded that only one pair of chains supported the low-temperature CDW. This point has not been fully resolved, although it does not affect the main results described here for the high-temperature screening modulations or the overall structure of the CDW at low temperature.

The impurities to be discussed here enter the $NbSe_3$ lattice in mostly interstitial positions unless there is a major phase change where the crystal structure changes and the impurity is incorporated into one of the chains. This generally means that the crystal grows, taking up an impurity concentration that is partially controlled by the preferred impurity modulation structure rather than the concentration introduced in the original sintered powder from which the crystal was grown. This often results in a substantially lower concentration in the final crystal than is introduced in the starting material. This has been quantitatively checked for Fe doping with secondary-ion-emission studies,[9] but for most of the doped crystals the residual resistance ratios are systematically monitored in order to compare the relative impurity concentrations. In addition, changes in the CDW resistance anomalies, CDW onset temperatures, CDW energy gaps at 4.2 K, and magnetoquantum oscillations at 1.1 K have been monitored. All of these show relatively small but systematic changes as the impurity concentration increases, although the changes produced for given ranges of concentration in the starting powder are specific for each type of impurity. The properties and specific modu-

0163-1829/95/51(19)/12975(14)/$06.00

lations scale with the values of x in the growth powder and are reproducible for crystals obtained from a given starting composition. We find that, as impurity levels are increased in the starting powders, the final crystals show a sequence of shifts that correspond to a monotonic increase of impurity concentration. The changes in the high-temperature modulation wavelength occur above certain critical impurity concentrations in the starting powder, and correlate with a higher density of impurities along the chains.

The above effects are to be distinguished from cases where above certain concentrations in the powder, the dopant replaces Nb and an attendant crystal structure change is induced. For example, crystals grown from Fe_xNbSe_3 powder with $x>0.10$ form crystals of $FeNb_3Se_{10}$ where the structure consists of four chains:[10] three $NbSe_3$ chains and one FeSe chain. In the case of Cr a sequence of $5\mathbf{b}_0$, $4\mathbf{b}_0$, $3\mathbf{b}_0$, and $2\mathbf{b}_0$ modulations is observed in the range $x=0.01-0.05$ followed by a sudden change in crystal structure at $x\geq 0.05$, where a phase can be observed which shows a metal-insulator transition[11] below 700 K and is insulating at room temperature. In these cases the CDW structure is completely changed and a much different analysis is required. Examples of AFM scans on these types of modified crystal phases will be presented in Secs. III A 7 and III A 8.

We will present AFM scans on $NbSe_3$ doped with a range of different impurities. All of them produce regular modulated structures at high temperatures, but the wavelengths, amplitudes, and profiles can be quite different. We also compare these high-temperature structures to changes observed in the CDW formation and energy gaps at low temperature as measured by resistance, STM scanning, and STM spectroscopy.

II. EXPERIMENTAL TECHNIQUES

The quasi-one-dimensional trichalcogenide crystals M_xNbSe_3 used in these experiments were grown in vacuum using sealed quartz tubes. Growth temperatures were in the range 700–800 °C with temperature gradient of ~15 °C per inch. The exact temperature and temperature gradient differ for each different compound. For these crystals, x refers to the M_x concentration relative to the Nb concentration in the original starting powder sintered in the presence of excess Se. The crystals grown from these powders are $NbSe_3$ with a concentration of M proportional to that contained in the original starting powder. The amount of M actually incorporated into the final crystals is systematically less than the nominal M_x concentration specified in the starting powder. However, all properties and modulations are reproducible for all crystals obtained from a given starting composition, and all these crystals are permanently stable at room temperature. The impurity concentration has been monitored by measuring the residual resistance ratio R and the quantum oscillation amplitude and frequency.

The AFM scans at room temperature have been made with commercial instruments Nanoscope II and III manufactured by Digital Instruments of Santa Barbara, CA. The constant force detecting mode is used throughout all these experiments.

III. EXPERIMENTAL RESULTS

A. AFM detection of modulated structures in doped $NbSe_3$ at 300 K

The long-range modulations in $NbSe_3$ induced by impurities have an amplitude on the order of 0.5–1.0 Å and can easily be detected in AFM scans of the cleaved crystal surface. Residual surface impurity atoms left after the cleave do not interfere with the AFM image and are either swept aside by the AFM tip or are no longer located in the area of several thousand square Å swept out in recording a typical image. The images shown have been Fourier filtered in order to eliminate noise, but the original unfiltered images clearly show the modulation structures being presented, and the Fourier transforms show very strong peaks at the wavevector of the observed modulation. For the impurities studied so far—vanadium, chromium, manganese, gadolinium, and palladium—a variety of modulations are observed as a function of concentration. Data on these five impurities will be presented first, followed by data on Fe and Co doping where the modulation wavelengths show less variation due to the relatively narrow range of impurity concentration that can be easily studied.

1. AFM scans of V_xNbSe_3 at 300 K

Vanadium produces ordered modulations in $NbSe_3$ for the entire range of concentration so far studied. Crystals have been grown from powders of the form V_xNbSe_3 where x varies from $x=0.01$ to 0.33 in the sintered powder. At $x=0.01$ a modulation of wavelength $6\mathbf{b}_0$ is observed as shown in the AFM scan of Fig. 1(a). The modulation of wavelength $6\mathbf{b}_0$ persists over the concentration range produced by powders with x in the range up to $x=0.11$. An AFM scan for a crystal grown with $x=0.11$ is shown in Fig. 1(b). The $6\mathbf{b}_0$ modulation is observed on all three chains of the surface unit cell with only small changes in the relative modulation amplitudes as the concentration increases in this range. However, the relative phase of the modulation on each adjacent chain does change as a function of concentration. At $x=0.01$ the phase between chains shifts slowly with six unit cells required for a phase shift of one period. At $x=0.11$ the phase shift between chains is much more rapid, with the shift of a complete period occurring between each surface unit cell containing three surface chains.

For x in the range above 0.11 the induced modulation changes wavelength from $6\mathbf{b}_0$ to $4\mathbf{b}_0$. An example of an AFM scan on a crystal grown from powder with $x=0.18$ is shown in Fig. 1(c). In this case the phase shift between each chain accumulates to a full period across each unit cell, as was the case for the $6\mathbf{b}_0$ modulation at $x=0.11$.

When x is increased to $x=0.33$ the modulation changes again and assumes a wavelength of $3\mathbf{b}_0$. An AFM scan on a crystal grown from a powder with

$x=0.33$ is shown in Fig. 1(d). In this case the modulation remains in phase on adjacent unit cells.

The profiles recorded along the chains for the four vanadium impurity concentrations represented in the scans of Figs. 1(a)–1(d) are shown in Figs. 2(a)–2(d). These show the atomic modulations within each period of the long-range modulation, and show the relative amplitudes of the long-range modulations. As the wavelength changes to shorter wavelengths the modulation amplitude of ~ 0.5 Å shows relatively small changes, indicating that the total charge modulation associated with the impurity screening remains approximately constant as the impurity spacing and screening modulation wavelength decrease.

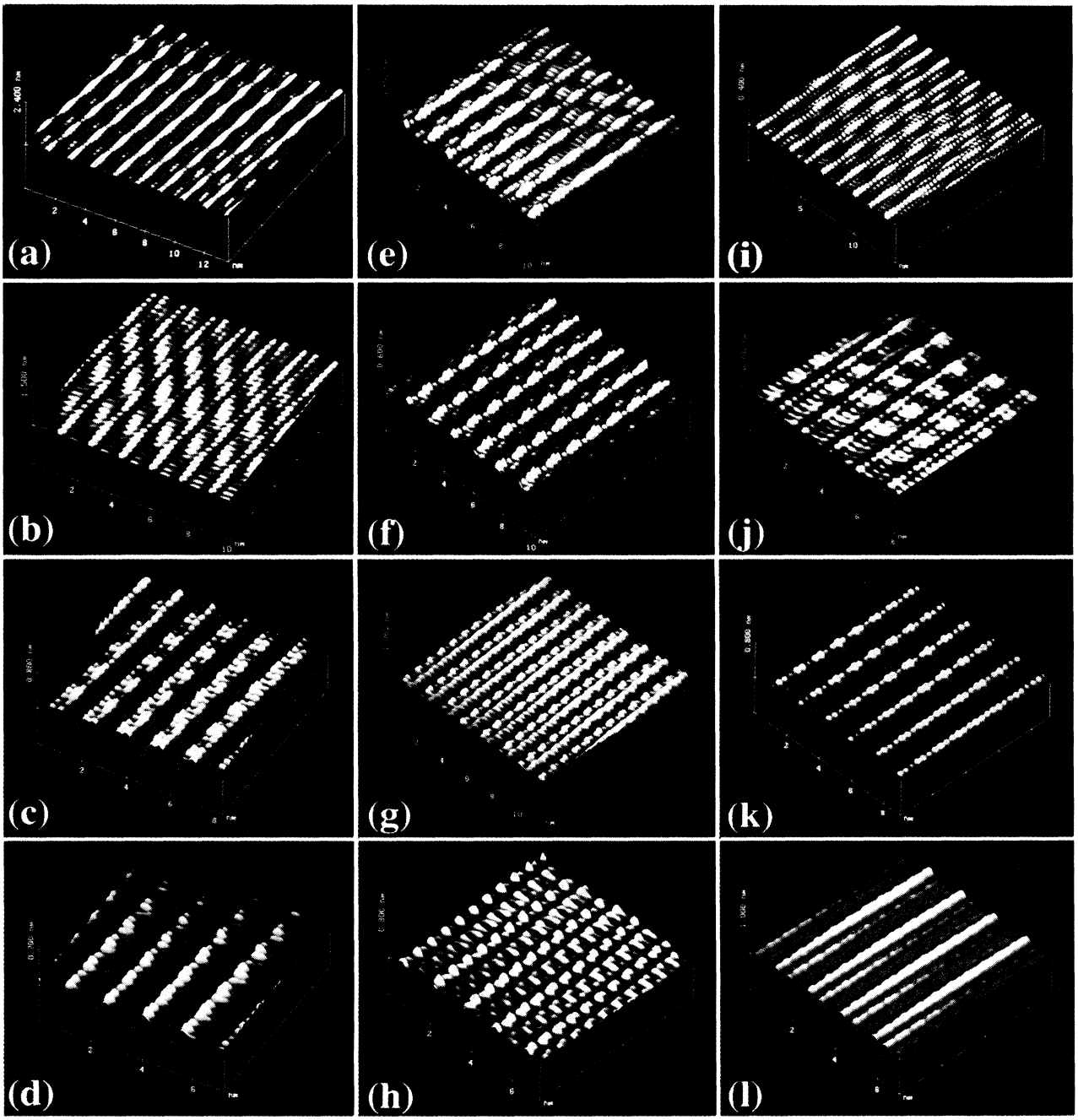

FIG. 1. AFM scans on V_xNbSe_3, Cr_xNbSe_3, and Mn_xNbSe_3 recorded using the constant force mode at room temperature. (a)–(d) V_xNbSe_3. A series of modulations with wavelengths $6b_0$, $6b_0$, $4b_0$, and $3b_0$ corresponding to $x=0.01$, 0.11, 0.18, and 0.33, respectively, are observed. (e)–(h) Cr_xNbSe_3. A series of modulations with wavelengths $5b_0$, $4b_0$, $3b_0$, and $2b_0$ corresponding to $x=0.01$, 0.01, 0.03, and 0.04 are present. (i)–(l) Mn_xNbSe_3. A series of modulations with wavelengths $8b_0$, $4b_0$, $3b_0$, and $2b_0$ corresponding to $x=0.03$, 0.10, 0.15, and 0.33 are shown.

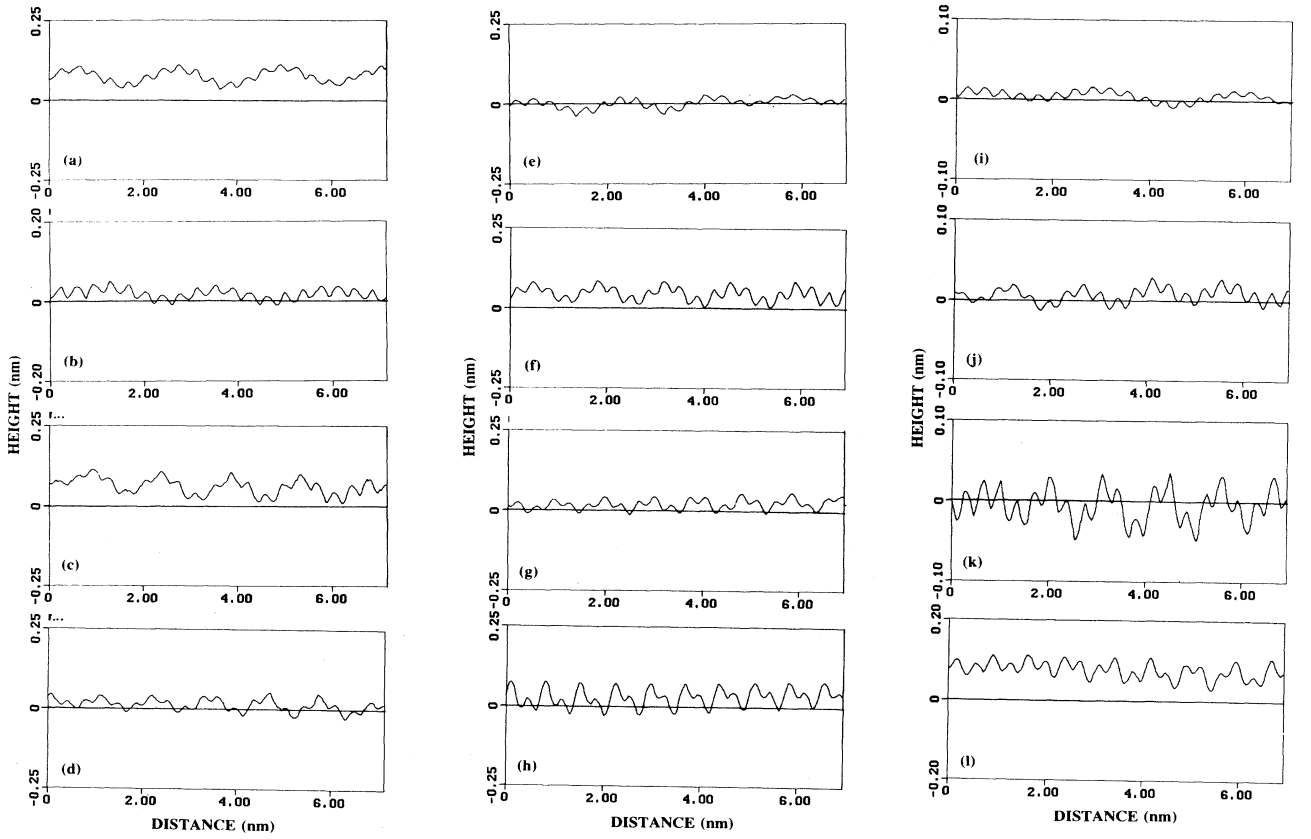

FIG. 2. Profiles of the modulations shown in Fig. 1 taken along the twofold axis (b axis). The precise atomic spacing of each long-range modulation is clearly shown. (a)–(d) V_xNbSe_3. (e)–(h) Cr_xNbSe_3. (i)–(l) Mn_xNbSe_3.

2. *AFM scans of Cr_xNbSe_3 at 300 K*

For Cr_xNbSe_3 crystals grown from powder with $x=0.01$ the AFM scans at room temperature show a long-range modulation of wavelength $5\mathbf{b}_0$ as shown in Fig. 1(e). The amplitude of the modulation is again on the order of 0.5 Å, as shown in the profile of Fig. 2(e). As the Cr concentration is increased modulations with wavelengths of $4\mathbf{b}_0$, $3\mathbf{b}_0$, and $2\mathbf{b}_0$ are observed as confirmed in the profiles of Figs. 2(f), 2(g), and 2(h). Examples of AFM scans recorded from crystals with $x=0.01$, 0.03, and 0.04 are shown in Figs. 1(f), 1(g), and 1(h). The rapid change of modulation wavelength with increase of Cr concentration in the starting powder can lead to the presence of more than one modulation wavelength in a given crystal due to local variations in the impurity density. These generally occur in different areas of the same crystal, but areas of overlap have been observed leading to beat structures in the AFM scans. The initial modulation of wavelength $5\mathbf{b}_0$ shows a phase shift of a full period over two unit cells. At higher impurity concentrations and shorter modulation wavelengths the modulation is approximately in phase on each unit cell.

3. *AFM scans of Mn_xNbSe_3 at 300 K*

The long-range impurity modulation induced by Mn doping of $NbSe_3$ behaves in a similar way to that observed for V doping as a function of concentration. At $x=0.3$ the modulation wavelength for Mn_xNbSe_3 is observed to be $8\mathbf{b}_0$, as shown in the AFM scan of Fig. 1(i) and the profile of Fig. 2(i). As the Mn concentration in the sintered growth powder is increased to $x=0.10$, 0.15, and 0.33, the modulation wavelength decreases to $4\mathbf{b}_0$, $3\mathbf{b}_0$, and $2\mathbf{b}_0$, respectively, as shown in the AFM scans of Figs. 1(j)–1(l) and the profiles of Figs. 2(j)–2(l). This is a different wavelength series than observed for V, but occurs over the same wide range of starting impurity concentration in the growth powder. The differences in modulation wavelength, phasing between chains, and the relative amplitudes of the different chains all must reflect the detailed charge defect and charge transfer characteristic of each specific impurity. This will be discussed in further detail in Sec. IV.

The phasing of the modulation between chains for Mn doping starts our requiring two unit cells for a phase shift of one modulation period of $8\mathbf{b}_0$. At the shorter modula-

tion wavelengths and higher impurity concentrations the phase shifts are smaller, and require a greater number of unit cells for a phase shift of one period. In this respect Mn is different from V, where in the later case the modulations at the shorter wavelengths and higher impurity concentrations were observed to be in phase after initially showing a phase shift between unit cells at the most dilute concentration ($x=6\mathbf{b}_0$) extending over six unit cells. The observed phase shifts of the impurity modulation between chains and unit cells is a function of both the concentration and the specific impurity, and a slightly different sequence seems to be observed for each separate impurity sequence.

4. *AFM scans of Gd_xNbSe_3 at 300 K*

The rare-earth impurity Gd modifies the electronic structure of $NbSe_3$ fairly rapidly, but at the most dilute concentrations in the starting growth powder a range of modulation wavelengths can be observed. For the lowest concentration studied corresponding to $x=0.01$ a long-range impurity modulation of wavelength $10\mathbf{b}_0$ is observed, as shown in Fig. 3(a) and the profile of Fig. 4(a). This is the longest impurity modulation wavelength observed so far, but longer-wavelength modulations can possibly be generated if crystals with lower concentrations can be prepared.

As the concentration of Gd in the growth powder is increased, the modulation wavelength decreases through a series of wavelengths $6\mathbf{b}_0$, $4\mathbf{b}_0$, and $2\mathbf{b}_0$, as shown in the AFM scans of Figs. 3(b)–3(d) and the profiles of Figs. 4(b)–4(d). These transitions in modulation wavelength occur within a range of concentration created by doping the growth powder with x in the range $x=0.003$–0.03. Some crystals show different modulation wavelengths in different areas of the crystal, indicating slightly different impurity concentrations.

We conclude that Gd is taken up rather rapidly by the growing crystal, and the rapid decrease in impurity screening modulation wavelength with increase in x confirms this. The changes in the low-temperature CDW resistive structure discussed in Sec. III C 4 and the changes in quantum oscillation frequencies reported in Ref. 12 also confirm this conclusion.

5. *AFM scans of Pd_xNbSe_3 at 300 K*

For the impurity modulations discussed in the previous sections the series of monotonically decreasing wavelengths have all been observed with differences that can be accounted for by differences in the charge Z_l on the impurity. The high-temperature modulations were observed to exist either over a large range of x or were ter-

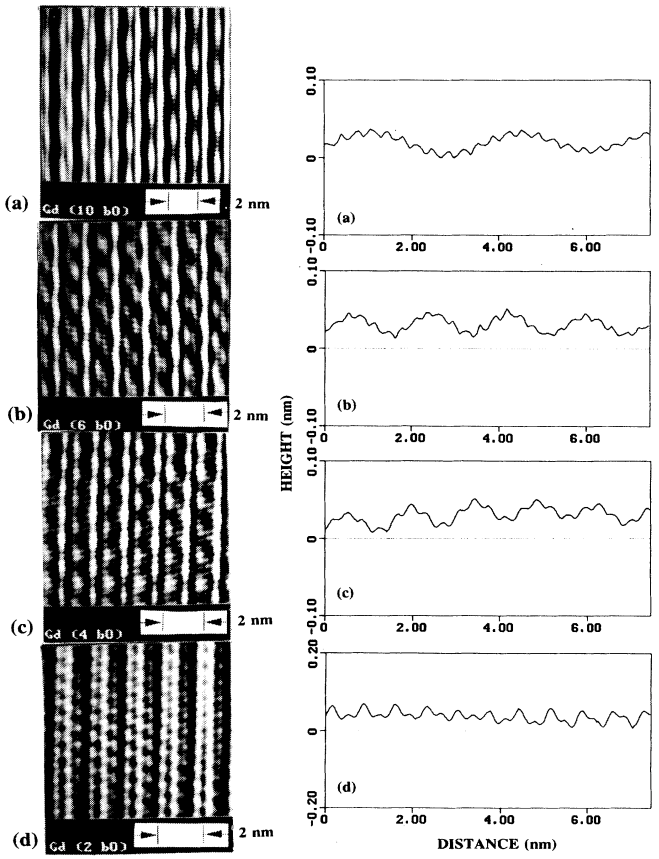

FIG. 3. AFM scans of Gd_xNbSe_3 for $x=0.003$–0.03 recorded using the constant force mode at room temperature. The images on the left and the profiles on the right show the wavelengths of impurity-induced modulations to follow a sequence of (a) $10b_0$, (b) $6b_0$, (c) $4b_0$, and (d) $2b_0$.

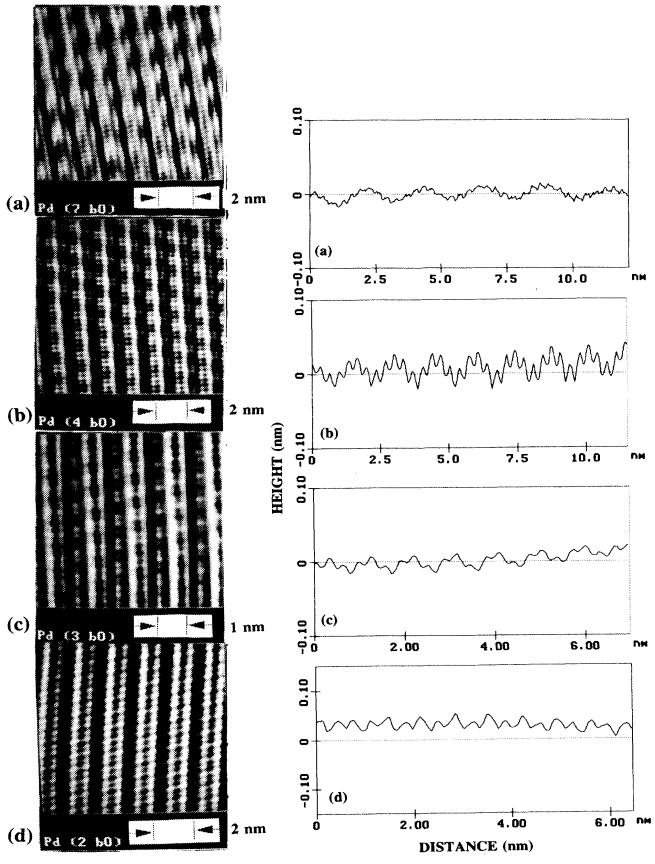

FIG. 4. AFM scans on the left and the profiles on the right of Pd_xNbSe_3 for $x=0.002$–0.01 recorded using the constant force mode at room temperature. The observed series of wavelengths of the long-range modulations is (a) $7b_0$, (b) $4b_0$, (c) $3b_0$, and (d) $2b_0$, as shown in (a)–(d).

minated by a phase change above some critical value of x. In all cases, the low-temperature CDW structure remained relatively unchanged in the range of x where the high-temperature modulation series were observed.

In the case of Pd doping a different situation exists in that the CDW structure can be quenched at a relatively low Pd concentration, and a phase change in the $NbSe_3$ crystal structure sets in a low concentration corresponding to an eight-chain structure instead of six-chain structure. At very dilute concentrations in the range $x=0.002-0.01$, the AFM scans show long-range impurity modulations very similar to those observed for the other impurities discussed above. As shown in the AFM scans of Fig. 4, the observed series of wavelengths is $7\mathbf{b}_0$, $4\mathbf{b}_0$, $3\mathbf{b}_0$, and $2\mathbf{b}_0$. However, for x between $x=0.02$ and 0.03 the CDW structure in Pd_xNbSe_3 is abruptly quenched, as will be shown in the resistance versus temperature curves of Sec. III C 1. AFM scans of $Pd_{0.03}NbSe_3$ show that the long-range impurity modulation has also vanished, as shown in the AFM scan of Fig. 5(a), where the three-surface-chain structure is still observed. The chains show an absolutely uniform modulation along the chain with a wavelength equal to the unit cell length of pure $NbSe_3$.

There is, however, a major change in the relative chain heights compared to those observed for pure $NbSe_3$. AFM scans on pure $NbSe_3$ at room temperature show chain III to be the highest chain as expected from the atomic structure (see Fig. 12). In contrast, the AFM scan on $Pd_{0.03}NbSe_3$ shows chain II to be the highest, with chain III at an intermediate height and chain I′ at the lowest height. This observation suggests a large charge transfer from the Pd to chain II, a feature which may be consistent with a band-structure change sufficient to quench the CDW structure. At higher concentrations the phase changes to a four-surface-chain structure as shown in Fig. 5(b) at 4.2 K in a STM scan and in Fig. 5(c) for an AFM scan at 300 K.

6. *AFM scans of Fe_xNbSe_3 and Co_xNbSe_3 at 300 K*

Doping of $NbSe_3$ with Fe and Co has so far been studied for a relatively narrow range of dilute concentrations corresponding to $x=0.01-0.03$ in the starting powder, with the exception of Co doping which has been extended to $x=0.10$. The modulation wavelength produced for both of these transition-metal impurities in the range studied is $2\mathbf{b}_0$. Examples of AFM scans for Fe and Co doping with $x=0.03$ and 0.10 are shown in Figs. 6(a) and 6(b). The $2\mathbf{b}_0$ wavelength seems to be the final wavelength obtained at higher concentrations for all impurities in the starting powder. This appears to represent the limit of interstitial impurity spacing, although modifications of the exact structure can occur as is the case for Cr_xNbSe_3 with $x=0.33$, to be discussed in Sec. III A 7.

The Fe and Co impurities modify the CDW energy gaps rapidly at dilute concentrations, and STM scans at 4.2 K show initial changes in the relative amplitudes of the two CDW's. These changes in CDW structure will be discussed in Sec. III C 6, but are relatively indepen-

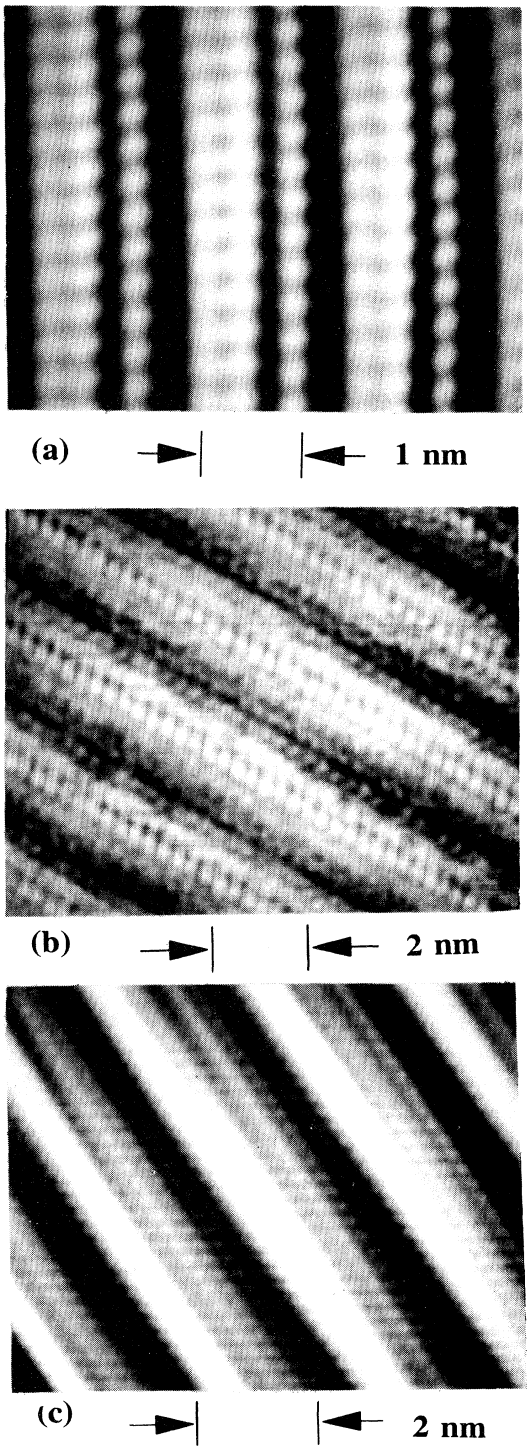

FIG. 5. (a) AFM scan on $Pd_{0.03}NbSe_3$ using the constant force mode at room temperature. No long-range modulation is present, although the crystal remains in three surface chains per unit cell structure. (b) STM images of $Pd_{0.10}NbSe_3$ taken at 4.2 K using the constant current mode ($I=2$ nA, $V=50$ mV). It shows a four-surface chain structure instead of three for pure $NbSe_3$. (c) AFM scan on $Pd_{0.10}NbSe_3$ using the constant force mode at room temperature. A four-surface chain structure is also observed.

dent of the impurity modulations observed at room temperature.

In the case of Fe for $x \geq 0.10$ the crystal structure changes to a four-chain structure which also exhibits a CDW. The effect of excess impurity on this phase will be discussed in Sec. III A 8. A similar sudden change in crystal structure is also observed for Cr_xNbSe_3 for $x=0.05$. This phase exists over a very narrow range of Cr concentration, and is discussed in Sec. III A 7.

7. *Metal-insulator transition in $Cr_{0.05}NbSe_3$*

As the Cr concentration in the starting powder approaches $x=0.05$, the crystal can grow into a phase characterized by a uniform chain structure and a strong modulation of wavelength $3\mathbf{b}_0$ as shown in Fig. 7(a). This phase has a different chain spacing and the unit-cell length along the chain is 4.3 Å versus 3.4 Å in pure $NbSe_3$. A slightly different crystal morphology can be detected in the optical microscope, although long needlelike crystals are formed. Crystals of this type are insulating at room temperature with a metal-insulator transition[11] between 600 and 700 K as shown in the resistance versus temperature curve of Fig. 8. The onset of the resistance rise occurs at ~700 K and the resistance has risen to 10 M Ω at 620 K followed by a completely insulating state at room temperature. The modulation at a wavelength of $3\mathbf{b}_0$ is extremely strong as shown in the profile of Fig. 7(b). The modulation occurs on every chain with a phase shift of ~120° between chains. The chains are uniformly spaced with a spacing of 6.5 Å.

As shown in the plane-view AFM scan of Fig. 7(a), the $3\mathbf{b}_0$ modulation of ~1-Å amplitude is identical on all surface chains, and each chain appears at the same height in the AFM scans. In this respect the chain structure and charge structure are completely different from those of the more dilute Cr-doped $NbSe_3$, where the chains are at different heights and the charge distribution associated with the long-range modulation are different on each chain of the unit cell consistent with dilute interstitial impurity modifications of the pure $NbSe_3$ unit cell.

Many crystals grown from powder with x in the range 0.04–0.05 remain conducting at room temperature and do not grow in the phase exhibiting a metal-insulator transition. These crystals show a mixture of $2\mathbf{b}_0$ and $3\mathbf{b}_0$

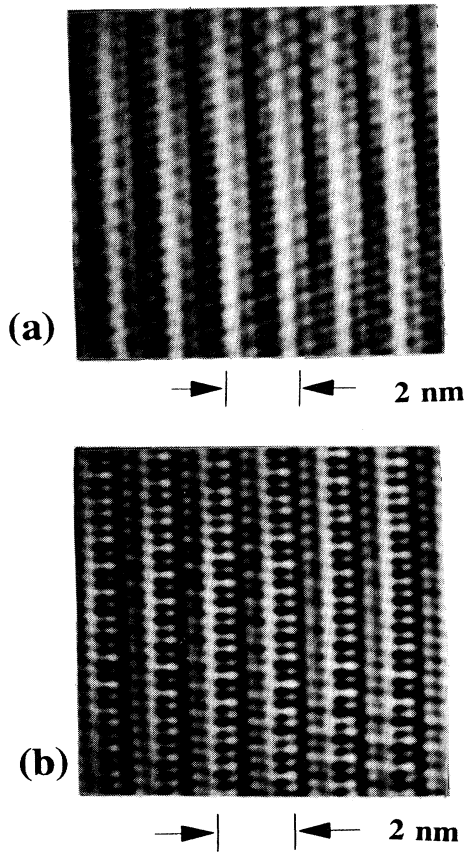

FIG. 6. (a) AFM scan on $Fe_{0.03}NbSe_3$. (b) AFM scan on $Co_{0.10}NbSe_3$. Both images are needed using the constant force mode at room temperature. They both show a modulation wavelength of $2b_0$.

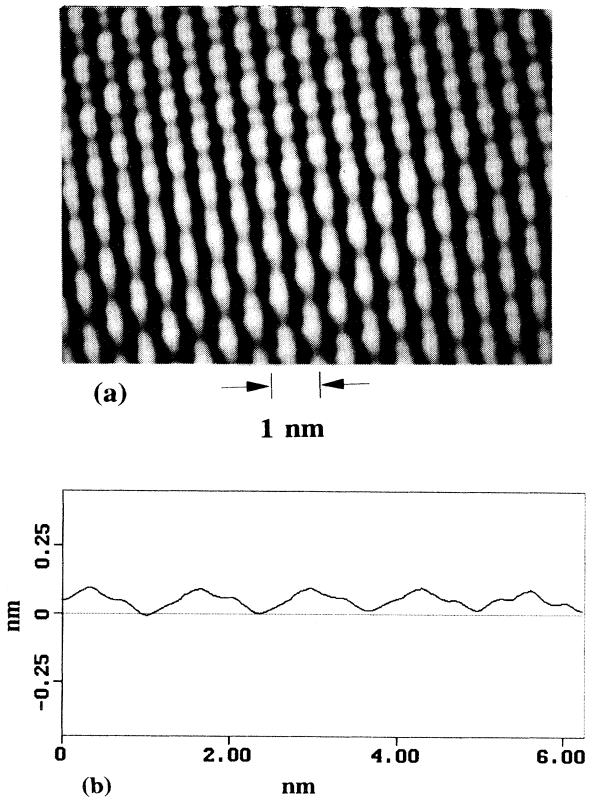

FIG. 7. (a) AFM scan at room temperature on $Cr_{0.05}NbSe_3$ recorded in the constant force mode. The image shows a large charge modulation along the **b** axis at a wavelength of approximately three atoms spacings. Each chain appears identical except for a phase displacement of 120° for the charge maxima on adjacent chains. This indicates three surface chains per unit cell for a superlattice. The chain spacing is 6.5 Å. The unit-cell length along the chain is 4.3 Å instead of 3.4 Å in pure $NbSe_3$. (b) Profile of z deflection taken along the chain. A $3b_0$ modulation is clearly seen, indicating that a CDW has formed in this phase.

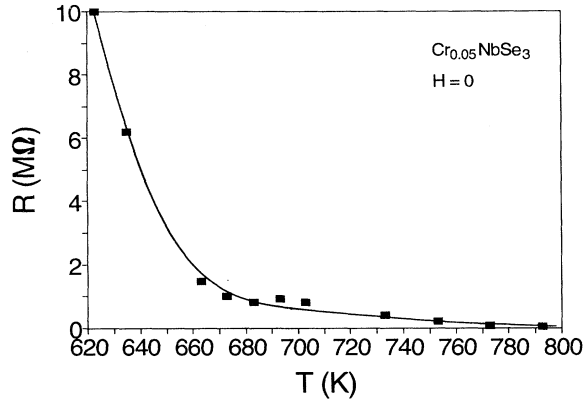

FIG. 8 Temperature dependence of resistance measured from 800–620 K for $Cr_{0.05}NbSe_3$. The crystal is a reasonably good metal at 800 K, while a strong metal-insulator transition is observed with an onset of ~700 K. At 620 K the resistance reaches 10 MΩ, and below 620 K the crystal rapidly becomes insulating.

modulations, and the low-temperature CDW structure remains characteristic of pure $NbSe_3$. The $3\mathbf{b}_0$ modulation in the insulating crystals is the only one observed and, although similar to that observed in the conducting crystals, it is much stronger and is uniform on all chains as emphasized above.

The experimental data seem to indicate that Cr impurities can be incorporated leading to either conducting or insulating states at room temperature for a same Cr concentration in the growth powder in the neighborhood of $x=0.05$. The conducting crystals remain in a crystal structure similar to that of pure $NbSe_3$ and show a mixture of screening modulations of wavelengths $3\mathbf{b}_0$ and $2\mathbf{b}_0$. The insulating phase corresponds to a crystal phase with a very strong $3\mathbf{b}_0$ modulation which is likely to be a different CDW formation associated with and driving the metal-insulator transition. This demonstrates how sensitive the electronic structure of $NbSe_3$ can be to the precise way in which dilute impurities are incorporated into the crystal structure.

The metal-insulator transition in dilute Cr-doped $NbSe_3$ is somewhat similar to those observed[13,14] in $FeNb_3Se_{10}$ or $Cr_{1.6}Nb_{2.4}Se_{10}$. However, the latter occur at much lower temperatures, on the order of 150 K, and these crystals do not go completely insulating even at 4.2 K. In addition, they have different crystal structures with only four chains per unit cell with Fe or Cr incorporated into the chains. In the case of $FeNb_3Se_{10}$ the metal-insulator transition is driven by a CDW which was clearly detected in x-ray-diffraction work.[13]

The experiments indicate that this insulating phase of Cr_xNbSe_3 exists for a very narrow range of Cr concentration and must correspond to a very special incorporation of Cr into the crystal structure. At Cr concentrations greater than the range of $x=0.05-0.06$, the crystals are observed to grow only in the pure $NbSe_3$ structure with the characteristic $2\mathbf{b}_0$ impurity modulation wavelength. As the concentration of Cr in the growth powder continues to increase, the charge distributions detected in the AFM scans show changes in spatial distribution, but remain at a wavelength of $2\mathbf{b}_0$. This indicates some change in the positions or concentration of Cr impurity in the unit cell, but the conclusion is that the local impurity concentration shows a very slow monotonic increase as x is increased in the range $x=0.05-0.25$.

At $x=0.33$ the Cr_xNbSe_3 crystals grow with a zigzag modulation predominantly located on two of the chains as shown in Fig. 9. The wavelength of this modulation is again $2\mathbf{b}_0$, but a larger component of distortion or charge transfer transverse to the chains has developed in contrast to the simpler modulation of wavelength $2\mathbf{b}_0$ observed for $x=0.03$ and 0.04. The chain spacing and unit-cell width remain approximately the same as observed for pure $NbSe_3$, demonstrating that the six-chain structure can accommodate interstitial impurities in a number of different preferred site configurations giving rise to ordered modulation along the chains, but having little or no effect on the low-temperature CDW structure.

8. *AFM scans on $FeNb_3Se_{10}$ at 300 K*

Crystals grown from powders with Fe concentrations in the range $x=0.10-0.50$ are found to grow in a four chain per unit cell monoclinic structure with Fe incorporated into two of the chains. The crystals of $FeNb_3Se_{10}$ are composed of two $NbSe_6$ trigonal prismatic chains and a double chain of edge-shared octahedral (Fe, Nb)Se_6.[10] These crystals undergo a metal-insulator transition with an onset temperature of 140 K. This metal-insulator transition was first detected by Hillenius *et al.*,[13] who observed a resistance rise of nine orders of magnitude between 140 and 3 K. It was also shown that a CDW transition occurred at 140 K with an incommensurate **Q** vector of $\mathbf{Q}=(0\mathbf{G}_a, 0.26\mathbf{G}_b, 0\mathbf{G}_c)$. Using pressure experiments Hillenius and Coleman[15] also showed that the metal-insulator transition was strongly correlated with the CDW formation, which allowed an Anderson type[16] of transition to occur below the CDW onset.

We have taken AFM scans on crystals grown from powders with nearly the correct stoichiometry of

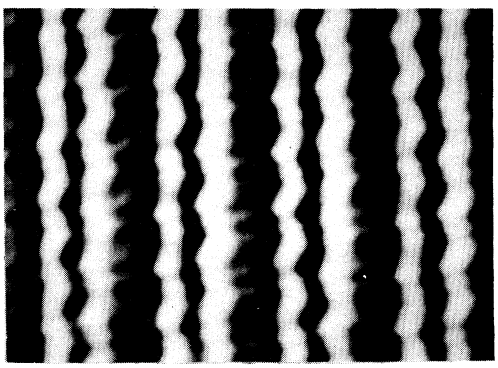

FIG. 9. AFM scan on $Cr_{0.33}NbSe_3$ recorded in the constant force mode at room temperature. A zigzag modulation pattern on two of the chains is observed. The overall modulation wavelength is still $2b_0$.

$Fe_{0.25}Nb_{0.75}Se_3$, and crystals grown from powders with a composition $Fe_{0.50}Nb_{0.75}Se_3$ corresponding to a substantial excess of Fe. AFM scans on crystals grown from stoichiometric powder show a uniform two-surface chain structure, as shown in Fig. 10(a). The crystals grown from the powder with excess Fe show a modulation of wavelength $2\mathbf{b}_0$ as shown in Fig. 10(b). We conclude that Fe has been included interstitially in the latter case, and that an impurity screening modulation similar to that observed in pure $NbSe_3$ crystals doped with interstitial Fe is being observed. This observation supports the conclusion that the impurity screening modulations detected by the AFM are characteristic of quasi-one-dimensional metals which form CDW's at lower temperatures, even though the CDW's exhibit different strengths and structure.

B. Comparison of AFM and STM scans on $NbSe_3$

The AFM measures the total charge density, while the STM measures the local density of states (LDOS) at the position of the tip associated with the conduction electrons. The surface scans by the two different instruments can therefore be quite different, particularly in the case of the impurity doped $NbSe_3$ crystals.

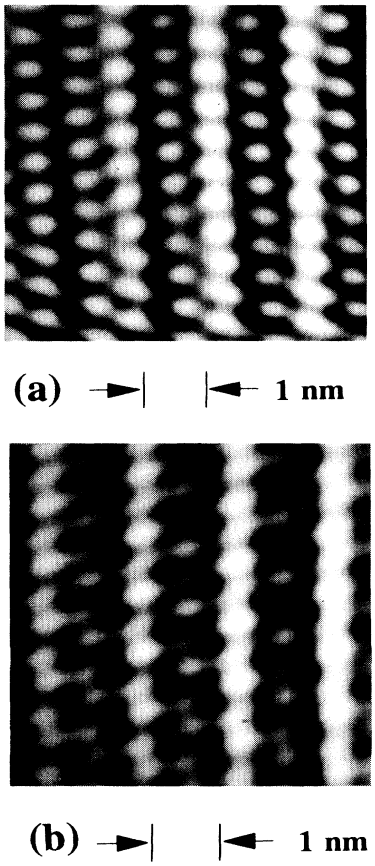

FIG. 10. (a) AFM scan on crystal grown for stoichiometric powder of $Fe_{0.25}NbSe_{0.75}Se_3$. A uniform two-chain surface structure is present. (b) AFM scan on crystal grown from the powder with excess Fe. A modulation of wavelength $2b_0$ is observed, indicating a long-range modulation associated with a susceptibility anomaly when interstitial impurities are present. Both images are taken in the constant force mode at room temperature.

Although direct quantitative connections between the two types of scans cannot be calculated, qualitative comparison can be useful in establishing the reliability and interpretation of the structures detected by the two instruments.

In this section we present such comparisons for some selected cases. In general the STM images are more difficult to obtain than the AFM images, since the STM is much more sensitive to surface work-function changes, defects both on the surface and below the surface, and to tip effects of various kinds. We also include some examples of STM scans at 4.2 K, although no AFM scans can presently be obtained at 4.2 K.

AFM and STM scans on pure $NbSe_3$

In order to establish the changes induced by impurities we have obtained both AFM and STM images of pure $NbSe_3$ at 300 K, as shown in Figs. 11(a) and 11(b). An overlay showing the surface structure of $NbSe_3$ has been superimposed on each scan. The AFM scan of Fig. 11(a) shows a much stronger static charge distribution on chain II than on chain I', although both are at the same height as shown in the unit cell diagram in Fig. 12. This is in agreement with the results of high-temperature band-structure calculations which show a substantially greater, net charge on chain II than on chain I'. Chain III shows a relatively strong localized charge, as expected since it is the highest chain.

STM scans, on the other hand, show a somewhat more uniform LDOS on all three chains with a very strong minimum in LDOS next to chain III corresponding to the large spacing between chains III and I' (see Fig. 12). The row of high Se atoms on chain III also creates a slightly more intense LDOS at the tip than do chains II and I'. The STM scans show a weaker response to differences in the static charge on the chains that do the AM scans, as expected. The LDOS at the Fermi level is only weakly affected by the self-consistent changes induced at the Fermi level by the tip and bias voltage, but the conduction electron wave function above the surface at the position of the tip can be more strongly modulated by the static surface charge. However, in general these effects are weaker in the STM than in the AFM, since the latter responds directly to the static charge at close range while the STM tip is at a greater distance in addition to responding indirectly via effects of the static charge on the LDOS at the position of the tip.

STM scans at 4.2 K on pure $NbSe_3$ show a somewhat similar picture, although the modulation along the chains is now dominated by the CDW modulation rather than the atomic modulation. As shown in Fig. 11(c), the very strong minimum between chains III and I' is still present, and in fact the scan is weakly detecting Se atoms on chain II' lying below the surface layer. Chains I' and II both show a very strong CDW modulation of the LDOS, while chain III is substantially weaker, consistent with

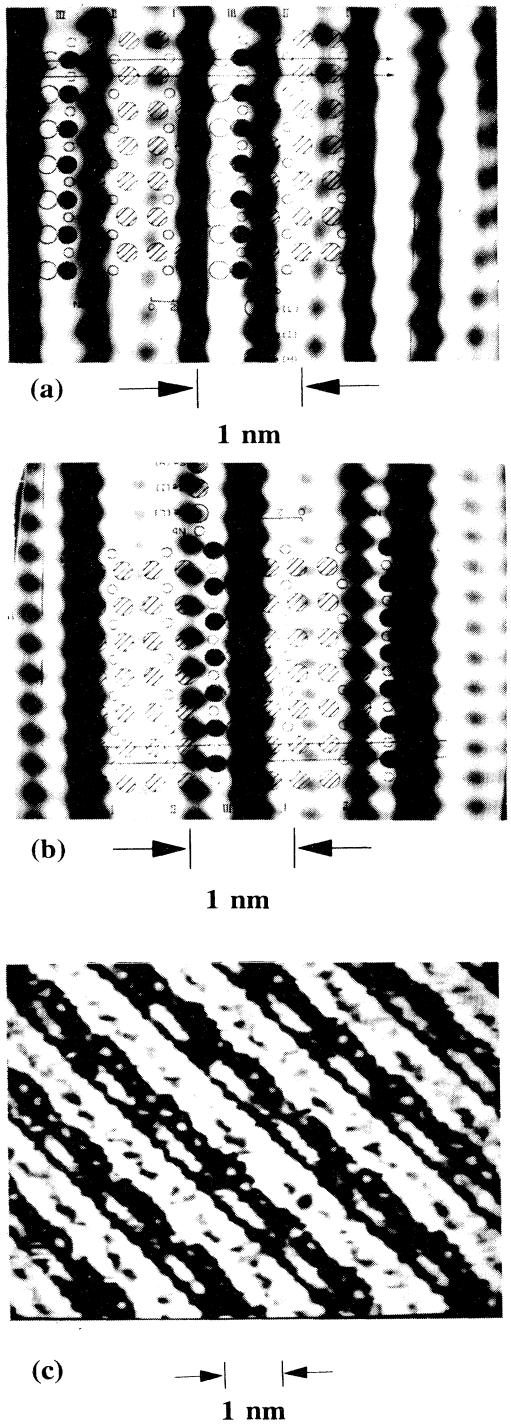

FIG. 11. (a) AFM scan on pure $NbSe_3$ recorded in the constant force mode at room temperature with an overlay showing the surface structure superimposed. It shows a much stronger static charge distribution on chain II than on chain I'. (b) STM scan of pure $NbSe_3$ recorded at room temperature using constant current model ($I=2$ nA and $V=20$ mV). The image shows a weaker response to differences in the static charge on the chains than AFM does. (c) STM scan of pure $NbSe_3$ recorded at 4.2 K using the constant current mode ($I=2$ nA, $V=50$ mV). CDW modulations of approximately $4b_0$ wavelength now dominate the image.

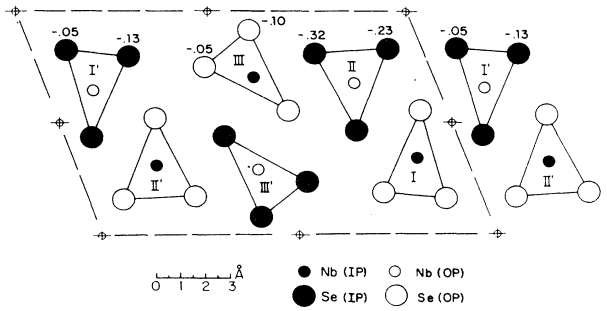

FIG. 12. Cross section of a $NbSe_3$ unit cell perpendicular to the chain axis (**b** axis). The solid atoms lie in the plane of the figure, and the open atoms are out of the plane.

the fact that the nearly perfect nesting of the Fermi surface associated with chain III has substantially reduced the conduction electron density on chain II.

Overall both the AFM and STM scans on pure $NbSe_3$ presented above show detailed structures which can reasonably be interpreted in terms of the atomic structure, charge structure, band structure, and CDW structure established both experimentally and theoretically for pure $NbSe_3$. The detailed changes induced by impurities as detected by both AFM and STM scans can therefore be reasonably interpreted as intrinsic changes in the locally averaged electric field at the surface in the case of the AFM, and changes in the LDOS at the position of the tip in the case of the STM. No evidence of any significant tip effects or distortions introduced by the instruments has been observed for the data reported here on images which satisfy both image quality and reproducibility. The results are also reproducible for repeated cleaves of the same crystal as well as for different crystals from the same growth tube.

C. Temperature dependence of resistance in impurity-doped $NbSe_3$

The long-range modulation observed at room temperature in doped $NbSe_3$ can be observed for many impurities and for a wide range of concentrations depending on factors such as the effective charge on the impurity. In all cases where room-temperature modulation is present, low-temperature CDW transitions are also observed, as can be verified in the resistance versus temperature curves. Figure 13 shows a selection of curves demonstrating the range of impurities and concentrations. In these cases the low-temperature CDW resistance anomalies are essentially unchanged from those observed in the pure materials. All the observations indicate that the existence of the high-temperature modulation in doped $NbSe_3$ requires that the low-temperature CDW transitions still exist when the crystal is cooled. In the following sections we summarize the results of the resistance versus temperature curves as a function of concentration for all of the dopants studied that show long-range high-temperature modulation.

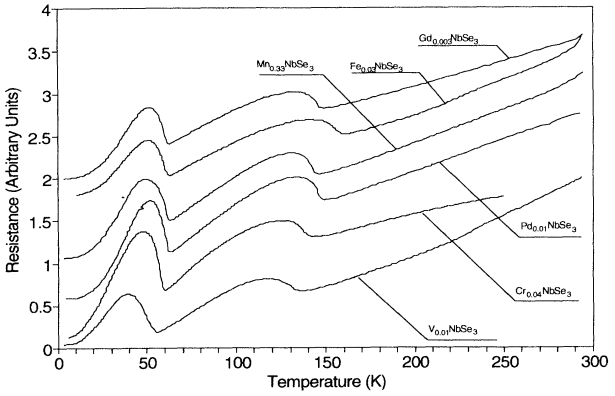

FIG. 13. Temperature dependence of resistance for a selection of impurity-doped $NbSe_3$ crystals. In these cases the low-temperature CDW resistance anomalies are essentially unchanged from those observed in pure $NbSe_3$.

1. *Resistance versus temperature for Pd_xNbSe_3*

Pd_xNbSe_3 is an example where at relatively low concentrations of Pd the CDW's are quenched after initially remaining unaffected by the addition of Pd. In this case, the electron transfer is sufficient to modify the electronic structure substantially as x increases from $x=0.02$ to 0.03, and at concentrations $x \geq 0.03$ the crystal structure switches over to an eight-chain unit cell. The resistance anomalies due to CDW formation are completely quenched as x increases above 0.03, as shown in Fig. 14.

The experiments in the transition region suggest that the low-temperature CDW transitions are quenched when the crystal is still in the six chain per unit cell structure, but switches very easily to the eight chain per unit cell structure for slight differences in concentration. As shown in Fig. 5(a) for a $Pd_{0.03}NbSe_3$ crystal in the six-chain structure (three surface chains), the high-temperature modulation is completely absent. As shown in Fig. 5(b), the $Pd_{0.03}NbSe_3$ crystals can show the eight-chain structure. Four double rows of atoms are shown in Fig. 5(b) and the c-axis unit-cell dimension is 23.7 Å rather than 15.4 Å in Fig. 1. The four-chain structure shows no long-range modulation, as expected.

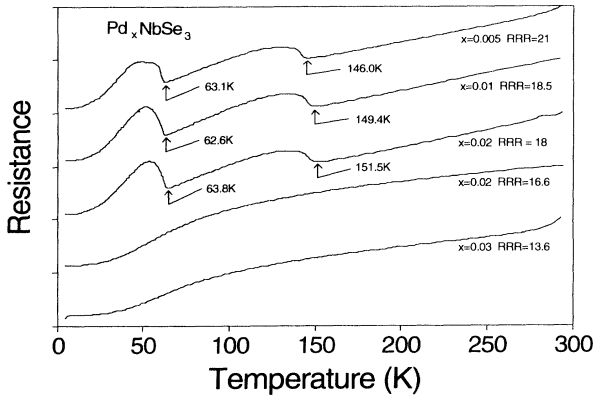

FIG. 14. Temperature dependence of resistance for Pd_xNbSe_3. For dilute Pd doping, the crystals of Pd_xNbSe_3 show little or no charge in the resistance anomalies associated with the low-temperature CDW transitions. In the range $x=0.02-0.03$ the low-temperature CDW resistance anomalies abruptly disappear.

2. *Resistance versus temperature for V_xNbSe_3*

The doping of $NbSe_3$ with V produces relatively small changes in the resistance anomalies associated with the two CDW's. However, the CDW onset temperature systematically decrease as the vanadium concentration is increased. Figure 15 shows a series of temperature dependence of resistance curves including the four concentrations present in the crystals used in the AFM scans of Fig. 1. For crystals grown from sintered powders with $x=0.01$ the CDW onset temperatures remain within a few degrees K of those observed for pure $NbSe_3$. The magnitudes of the resistance anomalies are also nearly the same as those observed for pure $NbSe_3$, but the residual resistance ratios R are reduced by more than an order of magnitude from a value in the range 200–300 to a value on the order of 5. As the value of x in the starting powder is increased, the CDW onset temperatures show a slow reduction which scales with the amount of V in the starting powder.

For $x=0.01$, 0.11, 0.18, and 0.33 the measured values $T_{C1}=137$, 123, 117, and 120 K and $T_{C2}=56$, 50, 47, and 47 K. The CDW resistance anomalies show a gradual reduction in magnitude but remain fairly strong. The largest change in resistance is observed at 4.2 K, where the resistance increases rapidly with increasing V concentration accounting for the dramatic reduction in R. This rise in resistance also interrupts the monotonic resistance drop observed below the resistance maximum associated with the low-temperature CDW.

The V-doping results presented in Secs. III A 1 and III C 2 above represent a system of distinct impurity modulations induced at high temperatures as function of the impurity concentration. These are accompanied by relatively slow monotonic changes in the CDW structure at

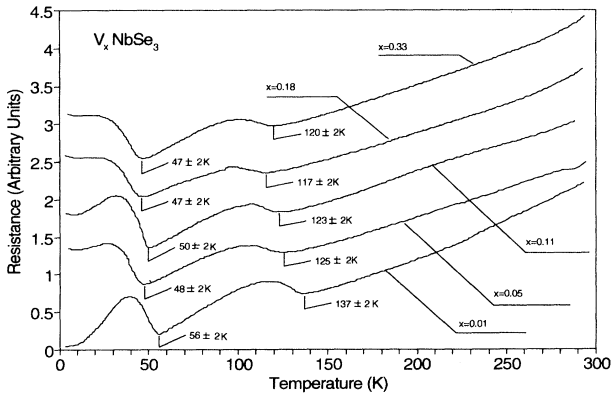

FIG. 15. Temperature dependence of resistance for V_xNbSe_3. The CDW onset temperatures systematically decrease as the vanadium concentration is increased.

low temperature. Other impurities in the dilute concentration range induce similar long-range modulations at high temperature, but can show more drastic modifications as the impurity concentration increases above certain limits. Examples will be presented below.

3. *Resistance versus temperature for Mn_xNbSe_3*

Doping of $NbSe_3$ with Mn produces a series of high-temperature modulations similar to those observed in V doping, but of slightly different wavelengths. Low-temperature CDW transitions are essentially unchanged over the entire concentration range as shown for $x=0.03$ and 0.33 in Fig. 16. This result is significantly different than observed for V doping where the T_C's of both CDW transitions are decreased substantially as the impurity concentration decreases. However, for both Mn and V doping the CDW resistance anomalies show a magnitude very similar to that observed in pure $NbSe_3$.

4. *Resistance versus temperature for Gd_xNbSe_3*

At the most dilute concentration Gd doping produces a high-temperature modulation of very long wavelength equal to $10\mathbf{b}_0$. This decreases rapidly through a series of wavelengths to $2\mathbf{b}_0$ as the Gd concentration is increased. In contrast to Mn doping, Gd produces very rapid changes in the shape of the CDW resistive anomalies as well as a rapid reduction in the T_C's of the resistance transitions, as seen in Fig. 17.

5. *Resistance versus temperature for Cr_xNbSe_3*

As pointed out in Sec. III A 7, Cr doping with x near 0.05 shows a phase with a metal-insulator transition. This is produced over a very narrow range of Cr concentrations. At much higher concentrations of Cr, Cr_xNbSe_3 shows low-temperature CDW transitions which are unchanged from those observed for the most dilute concentrations. Figure 18 compares resistance versus temperature curves for $x=0.04$ and 0.33 which are virtually identical. However, the high-temperature long-range modulations show a significant difference, as

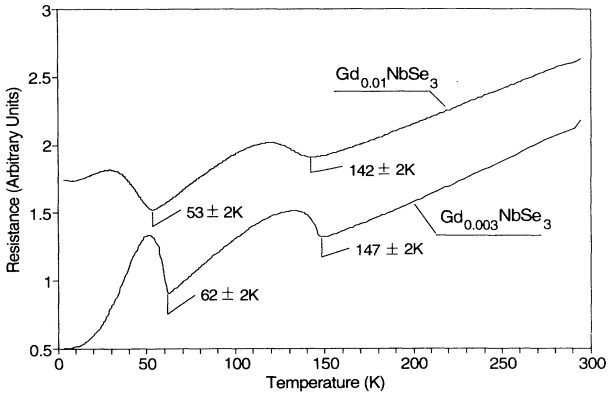

FIG. 17. Temperature dependence of resistance for Gd_xNbSe_3. Gd produces very rapid changes in the shape of the CDW resistive anomalies as well as a rapid reduction in the T_c's of the CDW transition.

was demonstrated in Fig. 9 where the high concentration doping produced a zigzag pattern of wavelength $2\mathbf{b}_0$.

6. *Resistance versus temperature for Fe_xNbSe_3 and Co_xNbSe_3*

Fe and Co produce high-temperature modulations of wavelength $2\mathbf{b}_0$ and at low concentrations do not modify the low-temperature CDW's. At $x=0.10$ Fe changes the crystal structure and enters the chain structure substitutionally. A metal-insulator transition is introduced, triggered by CDW formation at ~ 140 K. This is an unusual modification and is not induced by Co. No high-temperature modulation is observed for the Fe substitutional phase, although in this case the CDW anomaly is ten times[12] weaker than in pure $NbSe_3$. The resistance versus temperature behavior for the two dopants Fe and Co are shown in Fig. 19, which demonstrates the sensitive changes in both band structure and CDW structure which can be induced by impurities. For example at dilute concentrations Fe decreases low-temperature CDW

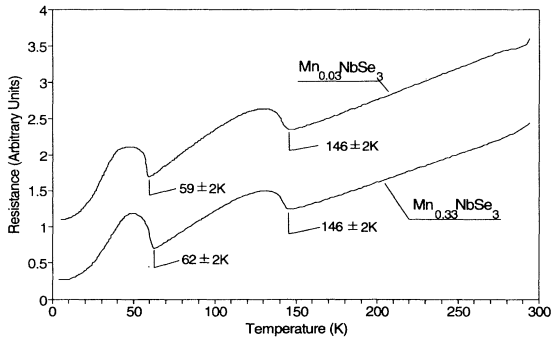

FIG. 16. Temperature dependence of resistance for Mn_xNbSe_3. The CDW onset temperatures are essentially unchanged over the entire concentration range from $x=0.03$–0.33.

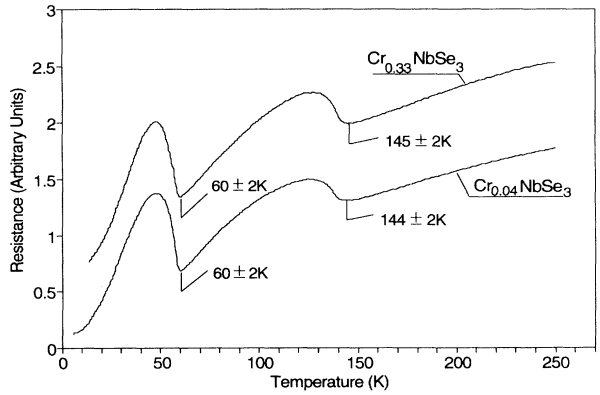

FIG. 18. Temperature dependence of resistance for Cr_xNbSe_3. The two curves with $x=0.04$ and 0.33 are virtually identical.

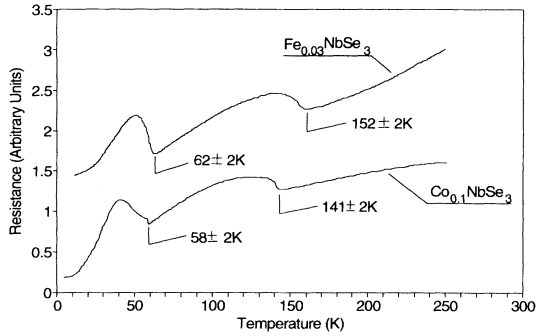

FIG. 19. Temperature dependence of resistance for $Fe_{0.03}NbSe_3$ and $Co_{0.10}NbSe_3$. Fe and Co introduce opposite changes in the CDW energy gaps of $NbSe_3$.

energy gaps, while Co increases the low-temperature CDW energy gaps. Data for CDW energy gaps have been presented and discussed in Refs. 17 and 18.

7. $Ti_xNb_{1-x}Se_3$

Ti is a substitutional impurity, and as expected tends to quench the low-temperature CDW's at a rapid rate as a function of concentration. The resistance versus temperature curves for dilute concentrations are shown in Fig. 20. No high-temperature modulations are observed, as shown in Fig. 21, possibly connected with the rapid quenching of the susceptibility anomalies. In this respect Ti and Gd doping both suppress the CDW's rapidly, but Gd shows a sequence of high-temperature modulations before the CDW's become quenched. Although many of the substitutional impurities have not been studied, the initial results suggest that only interstitial impurities produce high-temperature long-range modulations. The substitutional impurities introduce much less lattice strain and rapidly quench the low-temperature CDW anomalies.

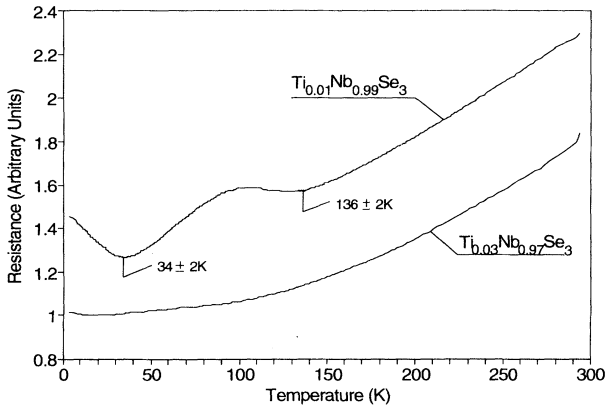

FIG. 20. Temperature dependence of resistance for $Ti_xNb_{1-x}Se_3$, where $x=0.01$ and 0.03. Ti quenches the low-temperature CDW's at a rapid rate as a function of concentration since Ti enters substitutionally in the chains.

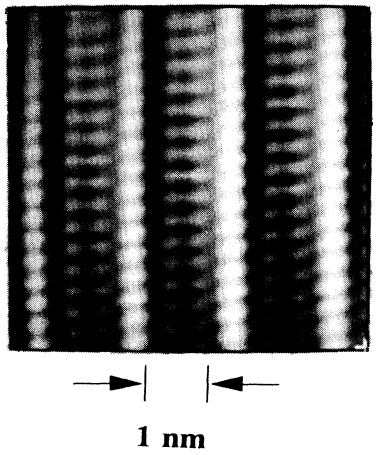

FIG. 21. AFM scan of $Ti_{0.03}Nb_{0.97}Se_3$ recorded in the constant force mode at room temperature. No impurity-induced long-range modulation is present.

IV. DISCUSSION

A. Impurity-induced modulation at room temperature

The AFM data presented in the previous sections show that the dilute interstitial impurities order along the chains with spacings that are multiples of the unit cell. This ordering of dilute impurities in the normal phase of a quasi-one-dimensional metal which undergoes a CDW transition at lower temperatures can be understood in terms of a recent phenomenological Ginzburg-Landau theory developed by Turgut and Falicov.[19]

The theory calculates a total trial free energy of a single infinite chain as a function of $n(x)$, the spatially dependent electronic charge density, and as a function of the impurity positions R_L and the impurity charges Z_L. The model uses the electronic charge density as the only order parameter, but takes into account the periodic lattice distortions (PLD's), since the PLD is a unique function of $n(x)$ and the impurity content and distribution $\{Z_L,R_L\}$. The PLD can be calculated when the real $n(x)$ and $\{Z_L,R_L\}$ are known.

In the normal state any impurity creates charge-density fluctuations that exhibit Friedel oscillations with wavelengths close to λ_c, the CDW wavelength at the transition. In the presence of several impurities, the electrons redistribute themselves on the chain, mostly in regions around the impurities, in the process screening the effective interaction between impurities. The model calculates the effects of the charge redistribution, the resulting electric fields, the screening interaction between impurities, and the dependence of the total free energy on the impurity distribution $\{Z_L,R_L\}$.

The interstitial impurities are assumed to be in a well-defined location in the unit cell, and the separation between two impurities is an integral multiple of the lattice constant a, since the variable $\{R_L\}$ refers only to unit cells which contain an impurity.

B. Effects on the low-temperature charge-density waves and the Fermi surface nesting

All of the dilute impurities at the lowest concentrations do not affect the formation of the two low-temperature CDW's. The onset temperatures show little or no shift and the resistance anomalies remain at the approximate magnitude observed for pure $NbSe_3$. However, as the concentration of the impurity is increased, changes occur depending on the specific impurity.

As outlined in Secs. III A–III C, the high-temperature modulation is observed to transition through a range of wavelengths as the impurity concentration is increased. This occurs for widely different doping concentrations for the different impurities, but as long as the high-temperature modulation is present the low-temperature CDW's show only small changes.

However, for selected impurities such as Cr and Pd both the high-temperature modulation and low-temperature CDW transitions disappear at relatively low concentrations. In the case of Cr crystal phase appears with a metal-insulator transition for a narrow range of initial concentration just above 5%. At much higher concentrations of Cr the high-temperature modulation and CDW transitions are restored, which indicates a reversion to the original $NbSe_3$ phase, but a slightly different impurity configuration.

In the case of Pd both the high-temperature modulation and the CDW transitions disappear above an initial concentration of between 2% and 3%, and are not reestablished at higher concentrations. In the Pd case the crystals remain in the $NbSe_3$ structure with six chains per unit cell even though the CDW transitions are quenched. This is a metastable structure and easily changes over into an eight chain per unit cell structure as outlined in Sec. III.

The observations indicate that not only do the impurities form a long-range modulation at high temperature, but also begin to induce band-structure changes and Fermi-surface modifications. The latter are very dependent on the specific impurity, and in a number of cases can induce a crystal phase transition.

V. CONCLUSIONS

The experiments reported here show that most dilute impurities in $NbSe_3$ produce a long-range modulation at high temperature of significant amplitude and wavelength that can be connected with the susceptibility anomaly that produces the low-temperature CDW transitions. Both coexist over the same range of concentration for a given impurity, although the high-temperature modulations progress to shorter wavelengths.

Both the high-temperature modulation and low-temperature CDW's disappear at critical concentrations where either the Fermi surface and band surface change or the crystal undergoes a phase transition. In the latter case a linear chain structure is formed with a variety of properties such as metal-insulator transitions. In some cases they are purely metallic without CDW's or long-range modulations.

The results show that $NbSe_3$ exhibits a delicately balanced electronic structure with CDW formation in the pure phase. Impurities initially are accommodated with an interesting long-range modulation. In some cases the electronic structure remains extremely stable against an increase in the impurity concentration, while in other cases an additional crystal structure is induced. This wide range of behaviors is closely connected with the existence of the susceptibility anomaly and the highly polarizable electron gas. The high-temperature modulations have been explained by the theory of Turgut and Falicov.

ACKNOWLEDGMENTS

This work has been supported by the U. S. Department of Energy, Grant No. DE-FG05-91ER45072, and by the National Science Foundation, Grant No. DMR92-23576. Useful discussions have been held with L. M. Falicov, V. Celli, and P. K. Hansma. Work in magnetic fields above 70 kG was performed at the Francis Bitter National Magnet Laboratory, supported at the Massachusetts Institute of Technology by the National Science Foundation. The authors wish to thank Larry Rubin and Bruce Brandt for valuable help with the experiments at the National Magnet Laboratory.

*Deceased.

[1]R. M. Fleming, D. E. Moncton, and D. W. McWhan, Phys. Rev. B **18**, 5560 (1978).

[2]*Charge Density Waves in Solids,* edited by L. P. Gor'kov and G. Gruner (North-Holland, New York, 1989).

[3]N. Shima and H. Kamimura, in *Theoretical Aspects of Band Structures and Electronic Properties of Pseudo-One-Dimensional Solids,* edited by H. Kamimura (Reidel, Boston, 1985), pp. 231–274.

[4]M.-H. Whangbo and P. Gressier, Inorg. Chem. **23**, 1305 (1984).

[5]Z. Dai, C. G. Slough, and R. V. Coleman, Phys. Rev. Lett. **66**, 1318 (1991).

[6]J. A. Wilson, Phys. Rev. B **19**, 6456 (1979).

[7]J. A. Wilson, J. Phys. F **12**, 2469 (1982).

[8]F. Devreux, J. Phys. (Paris) **43**, 1489 (1982).

[9]R. V. Coleman, M. P. Everson, H. Lu, A. Johnson, and L. M. Falicov, Phys. Rev. B **41**, 460 (1990).

[10]R. J. Cava, A. D. Mighell, V. L. Himes, and R. S. Roth, Phys. Rev. B **24**, 3634 (1981).

[11]Q. Xue, Z. Dai, Y. Gong, C. G. Slough, and R. V. Coleman, Phys. Rev. B **48**, 1986 (1993).

[12]R. V. Coleman, C. G. Slough, Z. Dai, Q. Xue, D. L. Drake, Y. Gong, and J. Qian (unpublished).

[13]S. J. Hillenius, R. V. Coleman, R. M. Fleming, and R. J. Cava, Phys. Rev. B **23**, 1567 (1981).

[14]A. Ben Salem, A. Meerschaut, H. Salva, Z. Z. Wang, and T. Sambongi, J. Phys. (Paris) **45**, 771 (1984).

[15]S. J. Hillenius and R. V. Coleman, Phys. Rev. B **25**, 2191 (1982).

[16]N. F. Mott, Philos. Mag. **19**, 835 (1969).

[17]Zhenxi Dai, C. G. Slough, and R. V. Coleman, Phys. Rev. B **45**, 9469 (1992).

[18]R. V. Coleman, Z. Dai, Y. Gong, C. G. Slough, and Q. Xue, J. Vac. Sci. Technol. B **12**, 1801 (1994).

[19]S. Turgut and L. M. Falicov, Phys. Rev. B **49**, 14 043 (1994).

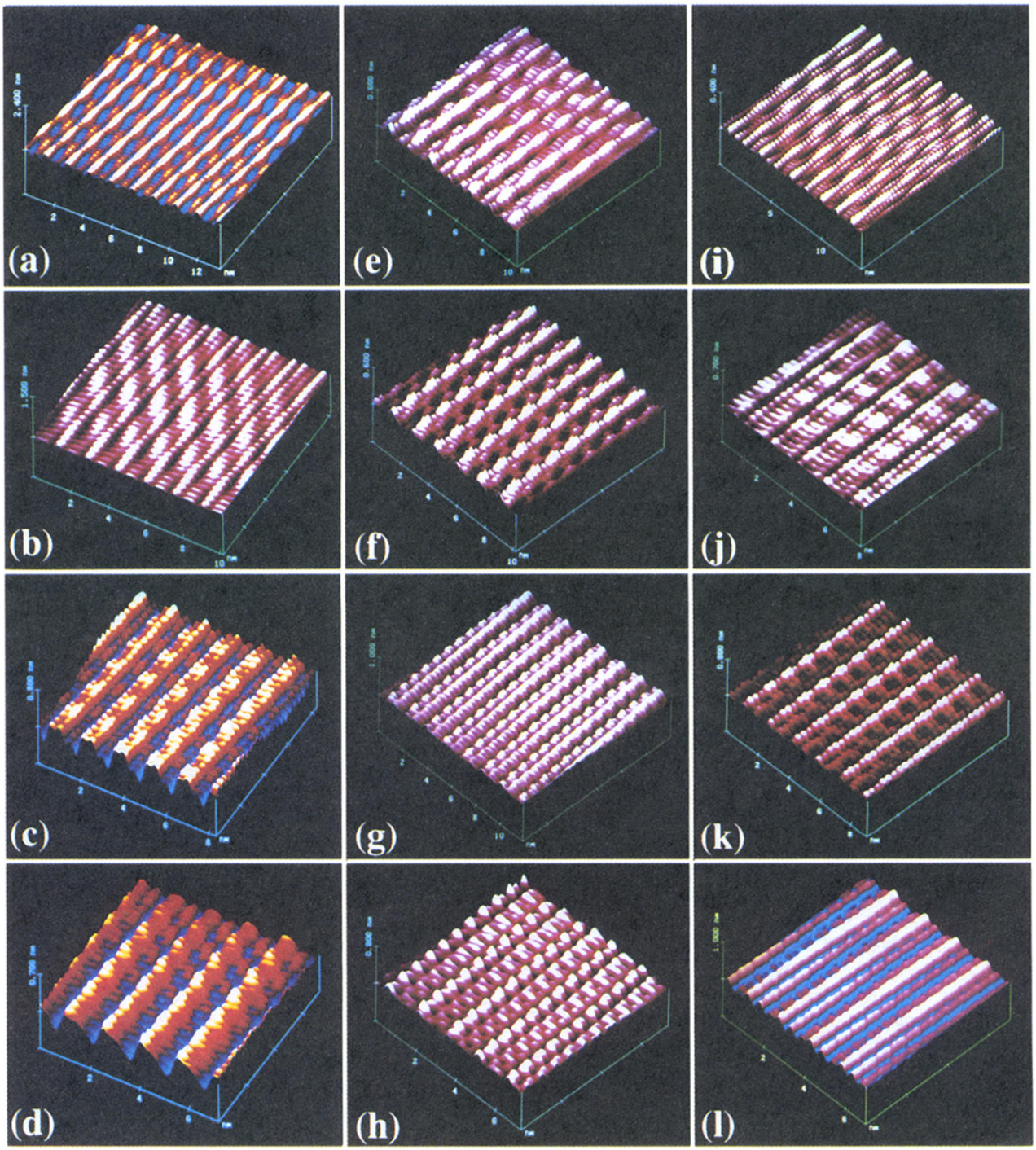

FIG. 1. AFM scans on V_xNbSe_3, Cr_xNbSe_3, and Mn_xNbSe_3 recorded using the constant force mode at room temperature. (a)–(d) V_xNbSe_3. A series of modulations with wavelengths $6b_0$, $6b_0$, $4b_0$, and $3b_0$ corresponding to $x=0.01$, 0.11, 0.18, and 0.33, respectively, are observed. (e)–(h) Cr_xNbSe_3. A series of modulations with wavelengths $5b_0$, $4b_0$, $3b_0$, and $2b_0$ corresponding to $x=0.01$, 0.01, 0.03, and 0.04 are present. (i)–(l) Mn_xNbSe_3. A series of modulations with wavelengths $8b_0$, $4b_0$, $3b_0$, and $2b_0$ corresponding to $x=0.03$, 0.10, 0.15, and 0.33 are shown.

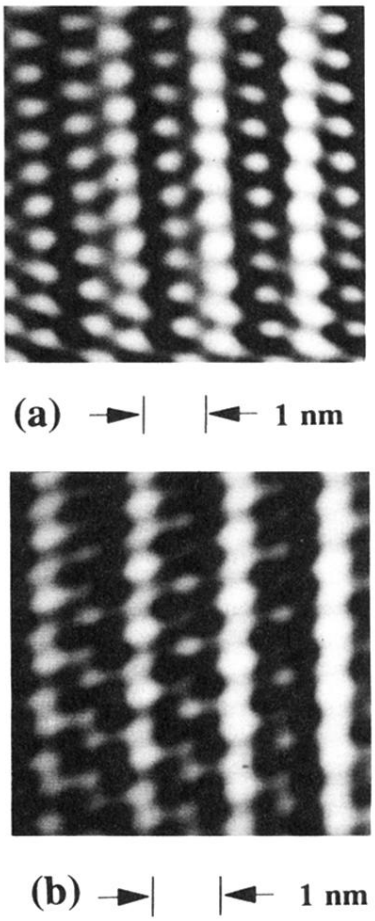

FIG. 10. (a) AFM scan on crystal grown for stoichiometric powder of $Fe_{0.25}NbSe_{0.75}Se_3$. A uniform two-chain surface structure is present. (b) AFM scan on crystal grown from the powder with excess Fe. A modulation of wavelength $2b_0$ is observed, indicating a long-range modulation associated with a susceptibility anomaly when interstitial impurities are present. Both images are taken in the constant force mode at room temperature.

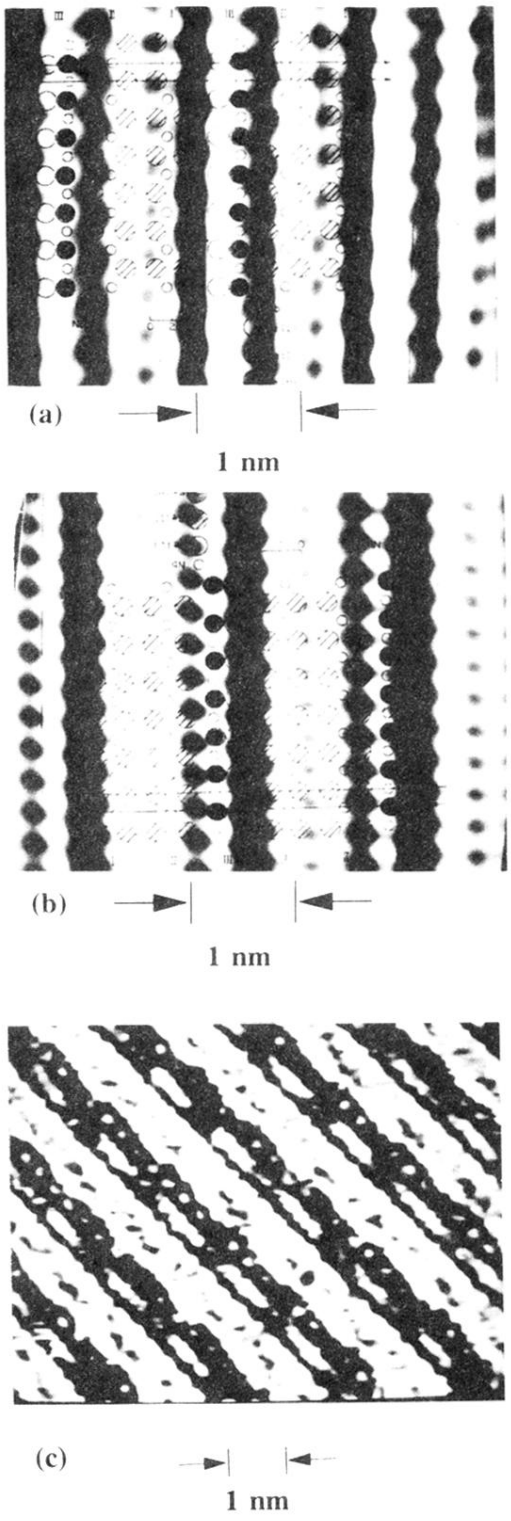

FIG. 11. (a) AFM scan on pure $NbSe_3$ recorded in the constant force mode at room temperature with an overlay showing the surface structure superimposed. It shows a much stronger static charge distribution on chain II than on chain I'. (b) STM scan of pure $NbSe_3$ recorded at room temperature using constant current model ($I=2$ nA and $V=20$ mV). The image shows a weaker response to differences in the static charge on the chains than AFM does. (c) STM scan of pure $NbSe_3$ recorded at 4.2 K using the constant current mode ($I=2$ nA, $V=50$ mV). CDW modulations of approximately $4b_0$ wavelength now dominate the image.

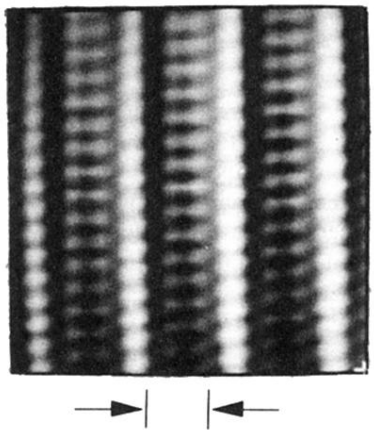

FIG. 21. AFM scan of $Ti_{0.03}Nb_{0.97}Se_3$ recorded in the constant force mode at room temperature. No impurity-induced long-range modulation is present.

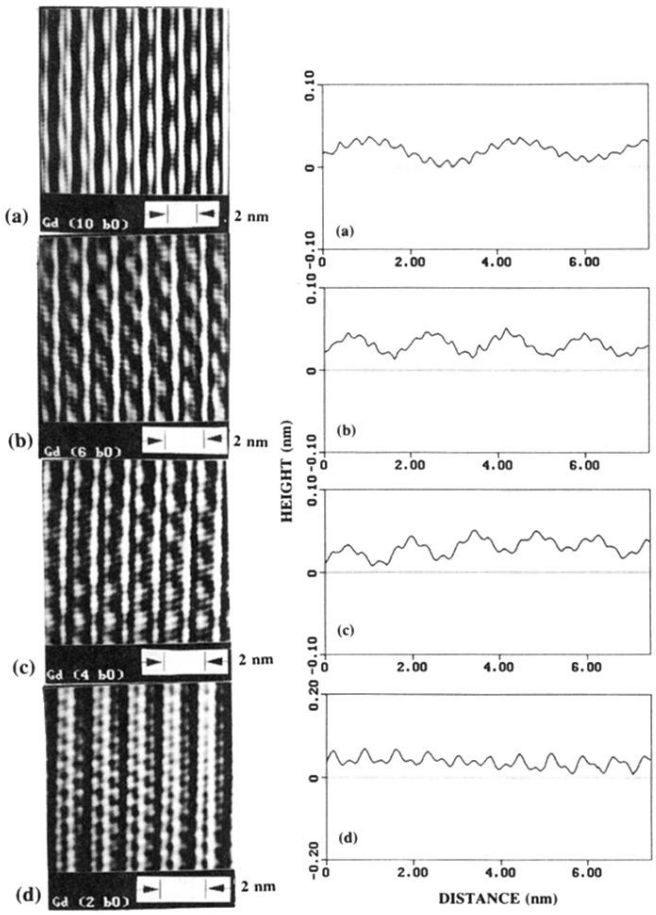

FIG. 3. AFM scans of Gd_xNbSe_3 for $x=0.003-0.03$ recorded using the constant force mode at room temperature. The images on the left and the profiles on the right show the wavelengths of impurity-induced modulations to follow a sequence of (a) $10b_0$, (b) $6b_0$, (c) $4b_0$, and (d) $2b_0$.

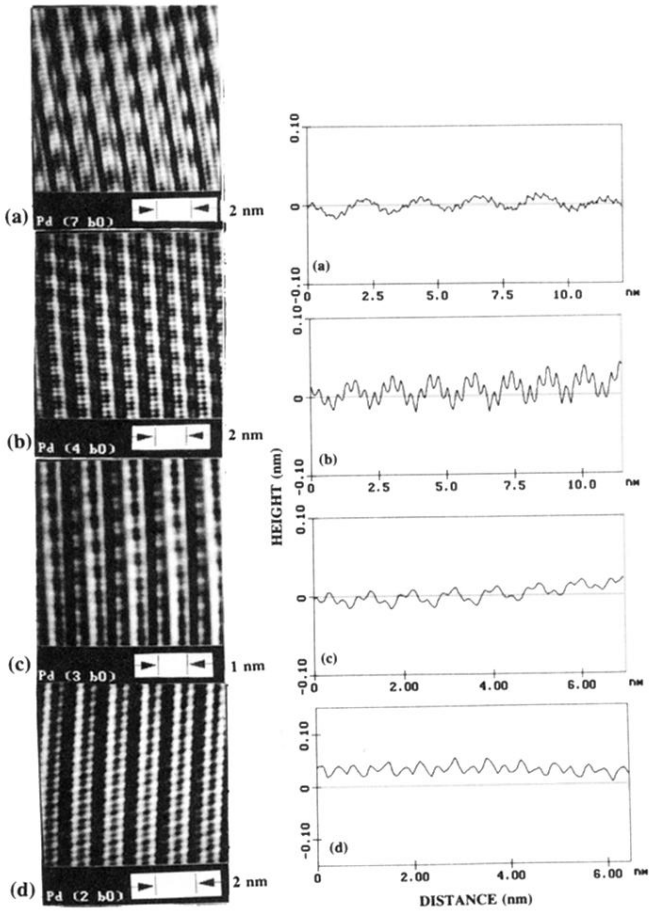

FIG. 4. AFM scans on the left and the profiles on the right of Pd_xNbSe_3 for $x=0.002-0.01$ recorded using the constant force mode at room temperature. The observed series of wavelengths of the long-range modulations is (a) $7b_0$, (b) $4b_0$, (c) $3b_0$, and (d) $2b_0$, as shown in (a)–(d).

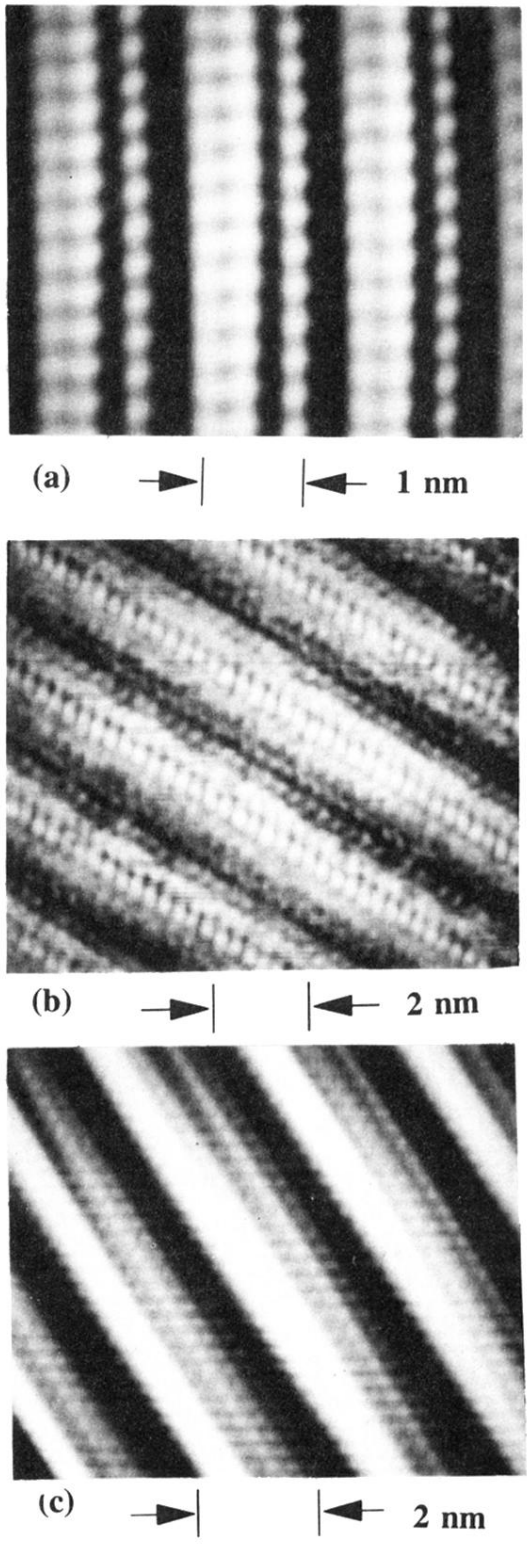

FIG. 5. (a) AFM scan on $Pd_{0.03}NbSe_3$ using the constant force mode at room temperature. No long-range modulation is present, although the crystal remains in three surface chains per unit cell structure. (b) STM images of $Pd_{0.10}NbSe_3$ taken at 4.2 K using the constant current mode ($I=2$ nA, $V=50$ mV). It shows a four-surface chain structure instead of three for pure $NbSe_3$. (c) AFM scan on $Pd_{0.10}NbSe_3$ using the constant force mode at room temperature. A four-surface chain structure is also observed.

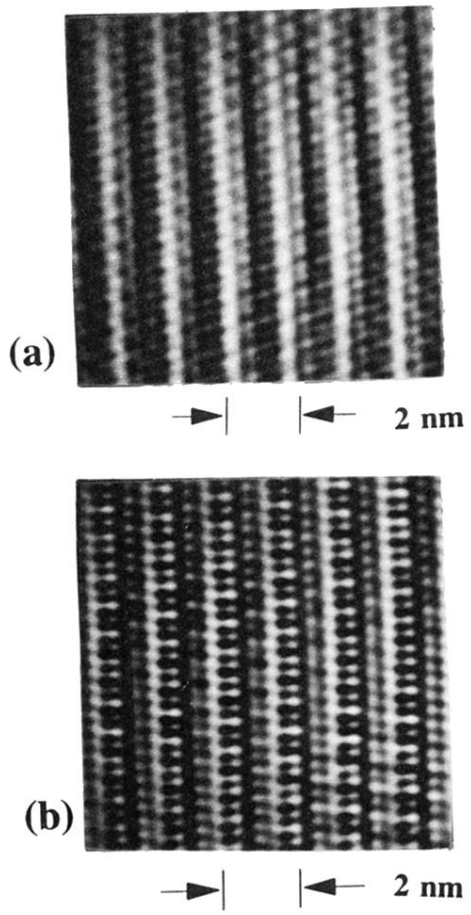

FIG. 6. (a) AFM scan on $Fe_{0.03}NbSe_3$. (b) AFM scan on $Co_{0.10}NbSe_3$. Both images are needed using the constant force mode at room temperature. They both show a modulation wavelength of $2b_0$.

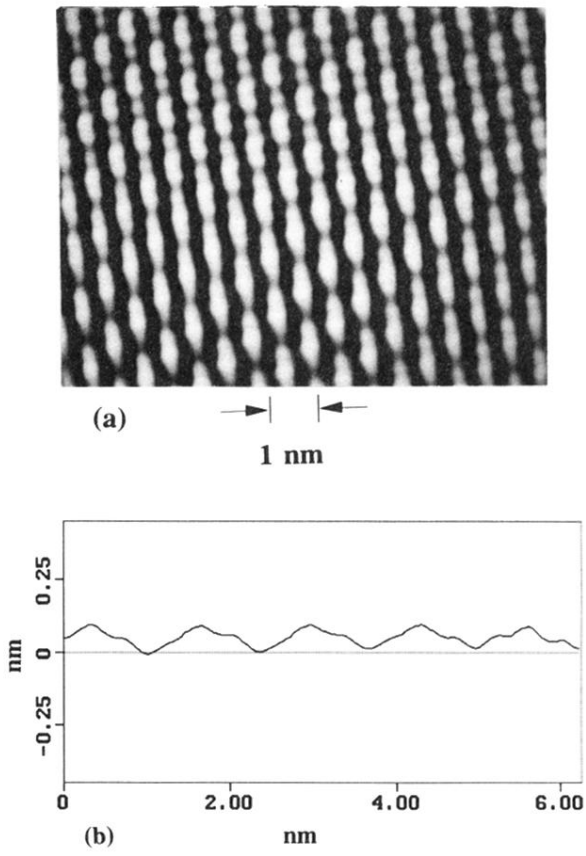

FIG. 7. (a) AFM scan at room temperature on $Cr_{0.05}NbSe_3$ recorded in the constant force mode. The image shows a large charge modulation along the **b** axis at a wavelength of approximately three atoms spacings. Each chain appears identical except for a phase displacement of 120° for the charge maxima on adjacent chains. This indicates three surface chains per unit cell for a superlattice. The chain spacing is 6.5 Å. The unit-cell length along the chain is 4.3 Å instead of 3.4 Å in pure $NbSe_3$. (b) Profile of z deflection taken along the chain. A $3b_0$ modulation is clearly seen, indicating that a CDW has formed in this phase.

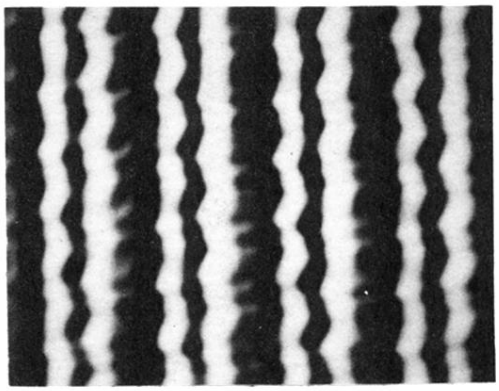

FIG. 9. AFM scan on $Cr_{0.33}NbSe_3$ recorded in the constant force mode at room temperature. A zigzag modulation pattern on two of the chains is observed. The overall modulation wavelength is still $2b_0$.